

Computation and Visualization of Three-Dimensional Soft Tissue Motion in the Orbit

Michael D. Abràmoff*, *Member, IEEE* and Max A. Viergever, *Member, IEEE*

Abstract—This work presents a method to measure the soft tissue motion in three dimensions in the orbit during gaze. It has been shown that two-dimensional (2-D) quantification of soft tissue motion in the orbit is effective in the study of orbital anatomy and motion disorders [1]. However, soft tissue motion is a three-dimensional (3-D) phenomenon and part of the kinematics is lost in any 2-D measurement. Therefore, T1-weighted magnetic resonance (MR) imaging volume sequences are acquired during gaze and soft tissue motion is quantified using a generalization of the Lucas and Kanade optical flow algorithm to three dimensions. New techniques have been developed for visualizing the 3-D flow field as a series of color-texture mapped 2-D slices or as a combination of volume rendering for display of the anatomy and scintillation rendering for the display of the motion field. We have studied the performance of the algorithm on four-dimensional volume sequences of synthetic motion, simulated motion of a static object imaged by MR, an MR-imaged rotating object and MR-imaged motion in the human orbit during gaze. The accuracy of the analysis is sufficient to characterize motion in the orbit and scintillation rendering is an effective visualization technique for 3-D motion in the orbit.

Index Terms—Cinematic MRI, multimodality visualization, optical flow, orbit.

I. INTRODUCTION

IT has been shown that the objective measurement of the motion of orbital soft tissue can improve the diagnosis and management of orbital disorders and may shed new light on the kinematics of orbital tissue [1], [2]. In these studies, a technique was introduced that uses cinematic magnetic resonance imaging (MRI) and optical flow computation of the motion field. This technique was limited to two dimensions. However, any technique based on two-dimensional (2-D) optical flow computation can only estimate the motion projected in the imaging plane. Since soft tissue motion and deformation is intrinsically three-dimensional (3-D) in nature, 3-D quantification may be beneficial. Problems for which 3-D quantification may be useful include the measurement of intraconal fat kinematics [3], measurement of muscle kinematics [4], and elucidation of the effect of muscle pulleys [5].

Manuscript received October 19, 2000; revised February 12, 2002. The work of M. D. Abràmoff was supported by the Dr. F. P. F. Stichting and the Department of Ophthalmology of the Vrije Universiteit University Hospital. The Associate Editor responsible for coordinating the review of this paper and recommending its publication was J. Prince. *Asterisk indicates corresponding author.*

*M. D. Abràmoff is with the Image Sciences Institute, University Medical Center Utrecht, Heidelberglaan 100, 3584 CX Utrecht, The Netherlands, and also with the Department of Ophthalmology, Room 4A65, Vrije Universiteit University Hospital, de Boelelaan 1117, 1081HV Amsterdam, The Netherlands (e-mail: michael@isi.uu.nl).

M. A. Viergever is with the Image Sciences Institute, University Medical Center Utrecht, 3584 CX Utrecht, The Netherlands.

Publisher Item Identifier S 0278-0062(02)04690-6.

This study introduces a method to analyze quantitatively and visualize 3-D motion and deformation. The method is based upon fast cinematic (cine) 3-D volumetric T1-weighted MRI in which hypervolumes (time series of volumes) are acquired during horizontal and vertical gaze. The 3-D motion present in the hypervolume is then analyzed with a 3-D optical flow algorithm. The algorithm is a 3-D generalization of the 2-D Lucas and Kanade optical flow algorithm, that was found to have the best performance on MR images [1]. A motion-to-color mapping was shown to be effective to visualize a 2-D-motion field in a small space [1] and this approach has been extended to create colored-textures that reflect the magnitude and orientation of the flow field in 3-D space. Other approaches to measure the motion in 3-D cine MRI sequences have been described, such as cine phase contrast (PC) MR [6] and MR-tagging [7]. Cine PC MRI utilizes the phase changes of the MR signals due to tissue motion [8]–[10]. Human heart motion has also been successfully estimated with MR-tagging [7], [11]. So far, cine PC MRI and tagged MRI have been studied in the context of heart and knee motion, with both relatively large and regular motion fields (combine to the motion in the orbit). There have been no studies comparing these methods, or applying their suitability to estimate motion at small scales.

A limitation to the proposed method is that cine MRI requires active cooperation from the patient. Since the main reason to undergo cine MRI is double vision or another ocular motility disorder, the number of MR acquisitions and the time allowed for them is necessarily severely constrained. This limits both the resolution of the volume and the number of volumes that can be acquired per motion sequence.

The purpose of this paper is to quantify objectively 3-D motion and deformation of soft tissues in the orbit. To this end, 3-D optical flow computation and 3-D motion visualization are introduced as techniques to analyze and present the measurement results. In view of the constraints outlined above, a side objective of the study is to establish whether the optical flow fields, thus, obtained are of sufficient quality to be clinically useful.

II. METHODS

A. MR Volume Acquisition

Cinematic MRI (3-D + time) hypervolumes were obtained using the following protocol. Gradient echo T1-weighted volumes were acquired on a 1.5-T MR scanner (Philips NT) using a head-coil with the following settings: turbo field echo, echo time (TE) 4.598 ms, repetition time (TR) 9.36 ms, flip angle 20°, and matrix 256 × 256 × 40, resulting in a voxel size of 0.8 × 0.8 × 2.0 mm and an acquisition time of 15 s per single volume for a single fixation position. The T1 relaxation times

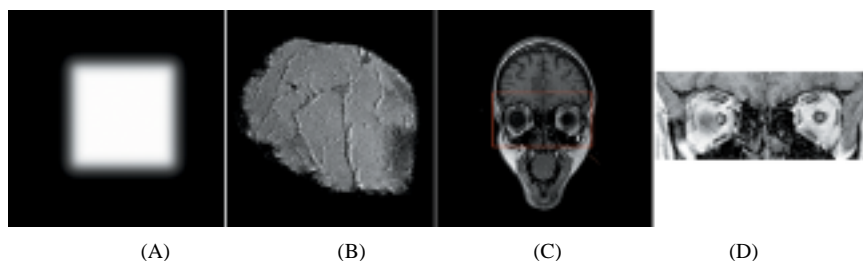


Fig. 1. Single slices from single volumes of the three objects imaged for this paper. (A) Single slice from single volume from *Cube* hypervolume ($60 \times 60 \times 60 \times 25$). (B) Single slice from *SteakMR* hypervolume ($256 \times 256 \times 40 \times 25$), central portion shown. (C) Single slice from *OrbitMR* hypervolume ($256 \times 256 \times 23 \times 9$). (D) Slice from *OrbitMR* Volume of Interest selected for motion estimations ($180 \times 50 \times 23 \times 9$).

were coded as signal intensities and the hypervolumes stored in DICOM 3.0 format as series of consecutive, separate images.

B. Simulated, Measured Hypervolumes

Since the true 3-D motion field in the orbit is unknown, simulations and MR measurements of controlled motion of an object were used to compare the flow field estimates with known motion fields. Simulated sequences were created by translating (at different velocities) a cube in 3-D space and obtaining $60 \times 60 \times 60 \times 25$ hypervolumes of the resulting motion sequence. We chose one of these for this study, called *Cube*.

Motion-controlled MR measured hypervolumes were obtained by rotating a sirloin steak in a transparent box fitted with an angle ruler as in [1] in the MR scanner bore. The phantom was manually rotated 5° per frame and $256 \times 256 \times 40 \times 25$ hypervolumes of the resulting motion sequence were obtained. We chose one of these for this study, called *SteakMR*.

In addition, a single MR volume of the sirloin steak was synthetically rotated 5° per frame using (tri-)linear interpolation, resulting in a $256 \times 256 \times 40 \times 9$ hypervolume of the resulting synthetic rotation sequence. We chose one of these for this study, called *SteakSynth*.

In the orbit, soft tissues undergo both rigid motion and (non-rigid) deformation. However, it is very difficult to evaluate experiments with deformation. This is because the deformation field cannot be objectively measured so as to provide the gold standard for the optical flow estimates. Therefore, we have synthetically simulated the 3-D deformation of a single MR volume of the sirloin steak, which resulted in a sequence called *SteakDeform*. The deformation simulated the impression of a rigid body (a ball of 3.0 mm) into the top of the steak, with the bottom of the steak being held fixed against a rigid plane over its entire width and being unrestrained at the sides. The ball impressed with 1.2 mm/frame. Tri-linear interpolation was used.

True orbital soft tissue motion hypervolumes were obtained by having a healthy subject fixate on sequential marks placed at 8° intervals along horizontal and vertical lines on the inside of the scanner bore. Each hypervolume thus acquired consists of a sequence of volumes ($256 \times 256 \times 23 \times 9$) of the resulting horizontal and vertical gaze motion sequences and each volume corresponds to a single gaze position. Three subjects were studied and we chose one of these sequences, called *OrbitMR*. Single slices of a single volume of each of the sequences are shown in Fig. 1.

III. OPTICAL FLOW COMPUTATION

A. Background

The optical flow field is a vector field that expresses the kinematic relationship between local 2-D or 3-D image samples [12]. Optical flow algorithms use the spatio-temporal patterns of these image or signal intensity samples to estimate the motion field. Optical flow computation has been used by several researchers for 2-D motion studies of MR sequences [13]–[16]. The Lucas and Kanade first-order differential algorithm is the most robust estimator of 2-D motion in MR sequences [1]. The starting point of optical flow computation is the optical flow constraint equation [12], [17]

$$\frac{dI(\mathbf{x}, t)}{dt} = 0 \quad (1)$$

where $I(\mathbf{x}, t)$ is the (possibly prefiltered) signal intensity series at location \mathbf{x} and time t and dI/dt the total derivative of I . Equation (1) expresses the assumption that structures do not change in signal intensity as they move. To make the optical flow vector \mathbf{v} explicit in the 3-D case, (1) can be expressed in terms of first-order partial derivatives as

$$\nabla I(\mathbf{x}, t) \cdot \mathbf{v} + I_t(\mathbf{x}, t) = 0 \quad (2)$$

with $\nabla I(\mathbf{x}, t)$ the gradient of I and $I_t(\mathbf{x}, t) = \partial I(\mathbf{x}, t)/\partial t$, the partial derivative of $I(\mathbf{x}, t)$ with respect to time. This is one equation with three unknowns, the components v_x, v_y , and v_z of the 3-D flow vector \mathbf{v} . Thus, this equation defines a plane for the normal component of the 3-D velocity vector. To solve (2) for \mathbf{v} , two additional constraints need to be introduced.

B. Three-Dimensional Optical Flow Algorithm

Lucas and Kanade over-constrained the 2-D version of (2) by assuming the flow to be regular over a small neighborhood. The 2-D motion vector can then be estimated by linear optimization from the over-constrained system of equations. By weighting the equations for the neighborhood with a Gaussian, the influence of neighboring (normal) flow vectors on the estimate is increased relative to that of vectors that are more distant. By generalizing this approach to three dimensions, the 3-D motion vector \mathbf{v} is estimated from a system of equations [each of the form of (2)] for the neighborhood Ω

$$\mathbf{AV} = \mathbf{b} \quad (3)$$

where, for $\mathbf{x}_i = 1 \dots m$, $\mathbf{x}_i \in \Omega$

$$\mathbf{A} = \begin{bmatrix} I_x(\mathbf{x}_1, t) & I_y(\mathbf{x}_1, t) & I_z(\mathbf{x}_1, t) \\ I_x(\mathbf{x}_2, t) & I_y(\mathbf{x}_2, t) & I_z(\mathbf{x}_2, t) \\ \vdots & \vdots & \vdots \\ I_x(\mathbf{x}_m, t) & I_y(\mathbf{x}_m, t) & I_z(\mathbf{x}_m, t) \end{bmatrix}$$

$$\mathbf{V} = \begin{bmatrix} v_x \\ v_y \\ v_z \end{bmatrix}$$

$$\mathbf{b} = -[I_t(\mathbf{x}_1, t), \dots, I_t(\mathbf{x}_m, t)]^T.$$

The system is weighted on both sides with a 3-D Gaussian W with standard deviation (of the associated probability function) σ_w

$$\mathbf{WAV} = \mathbf{Wb} \quad (4)$$

where, for $\mathbf{x}_i = 1 \dots m$, $\mathbf{x}_i \in \Omega$, $\mathbf{W} = \text{diag}\{W(\mathbf{x}_1), W(\mathbf{x}_2) \dots W(\mathbf{x}_m)\}$

The optimum solution for \mathbf{V} in (4), in a least squares sense, is obtained using the pseudoinverse [18]

$$\mathbf{V} = [\mathbf{WA}]^- \mathbf{Wb} \quad (5)$$

where $[\mathbf{WA}]^- = \text{pseudoinverse of } [\mathbf{WA}]$.

Provided $[\mathbf{A}^T \mathbf{WA}] \neq 0$, the pseudoinverse is identical to the least-squares inverse $[\mathbf{A}^T \mathbf{WA}]^{-1} \mathbf{A}^T$. The pseudoinverse can be found efficiently in closed form

$$\mathbf{A}^T \mathbf{WA} = \begin{bmatrix} \sum_{\mathbf{x} \in \Omega} W(\mathbf{x}) I_x^2 & \sum_{\mathbf{x} \in \Omega} W(\mathbf{x}) I_x I_y & \sum_{\mathbf{x} \in \Omega} W(\mathbf{x}) I_x I_z \\ \sum_{\mathbf{x} \in \Omega} W(\mathbf{x}) I_x I_y & \sum_{\mathbf{x} \in \Omega} W(\mathbf{x}) I_y^2 & \sum_{\mathbf{x} \in \Omega} W(\mathbf{x}) I_y I_z \\ \sum_{\mathbf{x} \in \Omega} W(\mathbf{x}) I_x I_z & \sum_{\mathbf{x} \in \Omega} W(\mathbf{x}) I_y I_z & \sum_{\mathbf{x} \in \Omega} W(\mathbf{x}) I_z^2 \end{bmatrix} \quad (6)$$

with $I_x = I_x(\mathbf{x}, t)$ etc., so that

$$\mathbf{A}^T \mathbf{Wb} = \begin{bmatrix} \sum_{\mathbf{x} \in \Omega} W(\mathbf{x}) I_x I_t \\ \sum_{\mathbf{x} \in \Omega} W(\mathbf{x}) I_y I_t \\ \sum_{\mathbf{x} \in \Omega} W(\mathbf{x}) I_z I_t \end{bmatrix} \quad (7)$$

and

$$[\mathbf{A}^T \mathbf{WA}]^{-1} = \begin{bmatrix} \frac{\Xi_{yy} \Xi_{zz} - \Xi_{yz}^2}{[\mathbf{A}^T \mathbf{WA}]} & \frac{\Xi_{xz} \Xi_{yz} - \Xi_{xy} \Xi_{zz}}{[\mathbf{A}^T \mathbf{WA}]} & \frac{\Xi_{xy} \Xi_{yz} - \Xi_{xz} \Xi_{yy}}{[\mathbf{A}^T \mathbf{WA}]} \\ \frac{\Xi_{xz} \Xi_{yz} - \Xi_{xy} \Xi_{zz}}{[\mathbf{A}^T \mathbf{WA}]} & \frac{\Xi_{xx} \Xi_{zz} - \Xi_{xz}^2}{[\mathbf{A}^T \mathbf{WA}]} & \frac{\Xi_{xy} \Xi_{xz} - \Xi_{xx} \Xi_{yz}}{[\mathbf{A}^T \mathbf{WA}]} \\ \frac{\Xi_{xy} \Xi_{yz} - \Xi_{xz} \Xi_{yy}}{[\mathbf{A}^T \mathbf{WA}]} & \frac{\Xi_{xy} \Xi_{xz} - \Xi_{xx} \Xi_{yz}}{[\mathbf{A}^T \mathbf{WA}]} & \frac{\Xi_{xx} \Xi_{yy} - \Xi_{xy}^2}{[\mathbf{A}^T \mathbf{WA}]} \end{bmatrix} \quad (8)$$

with $\Xi_{xy} = \sum_{\mathbf{x} \in \Omega} \{W(\mathbf{x}) I_x(\mathbf{x}, t) I_y(\mathbf{x}, t)\}$, so that \mathbf{V} can be evaluated analytically. This is important for an acceptable performance, since otherwise $[\mathbf{A}^T \mathbf{WA}]^{-1} \mathbf{A}^T$ would have to be computed iteratively.

In the discrete case, the partial derivatives of I , I_j , where $i \in \{x, y, z\}$, are of dimension $length^{-1}$, so that the derivative products of the matrix in (6) have dimension $length^{-2}$. The eigenvalues λ_1 , λ_2 , and λ_3 , with $\lambda_1 > \lambda_2 > \lambda_3$, of (6) form a metric for the regularity of the (gradients in the) neighborhood Ω and are used as a reliability index as in [19]. If λ_3 is larger than a threshold τ (of dimension $length^{-2}$), the flow in Ω is

TABLE I
4-D "SOBEL" DIFFERENTIATION KERNEL

		z-1			z			z+1		
		x-1	x	x+1	x-1	x	x+1	x-1	x	x+1
t-1	y-1	-2	0	2	-3	0	3	-2	0	2
	y	-3	0	3	-6	0	6	-3	0	3
	y+1	-2	0	2	-3	0	3	-2	0	2
t	y-1	-6	0	6	-9	0	9	-6	0	6
	y	-9	0	9	-18	0	18	-9	0	9
	y+1	-6	0	6	-9	0	9	-6	0	6
t+1	y-1	-2	0	-3	-3	0	3	-2	0	2
	y	-3	0	3	-6	0	6	-3	0	3
	y+1	-2	0	2	-3	0	3	-2	0	2

assumed to be regular in 3-D and \mathbf{v} is assumed to be reliable. If λ_2 is larger than τ , but not λ_3 , the flow in Ω is assumed to be regular in two dimensions only and the normal of \mathbf{v} is obtained by projecting the result of (5) onto the eigenvector associated with λ_1 (the largest eigenvalue). Many structures in the orbit do not have a 3-D texture, but a predominantly 2-D texture, such as blood vessels and nerves. If strict 3-D regularity is imposed on the motion of these structures, the normal of \mathbf{v} cannot be used to give an indication of the motion.

C. Derivative Computation

The quality of the optical flow field computed by the above method depends on the accuracy of the partial derivatives $\partial I / \partial x$, $\partial I / \partial y$, $\partial I / \partial z$, and $\partial I / \partial t$ in (2), which are obtained from the (discrete) motion sequences [19]. As mentioned above, due to the clinical constraints, the hypervolumes that contain the 3-D MRI motion sequences are aliased both spatially and temporally. In [1], we have examined the 2-D performance of three forms of derivative computation, using central difference kernels, Sobel 2-D + time derivative kernels and Gaussian derivatives. In that study, Gaussian derivatives [20] were found to have the best performance. The continuous form of the Gaussian derivative kernel is given by

$$G(x) = e^{-x^2/(2\sigma^2)} \text{ and } G'(x) = -\frac{1}{\sigma^2} x e^{-x^2/(2\sigma^2)}. \quad (9)$$

The temporal and spatial components of the scale σ of the Gaussian and its derivative in (9) were separated as σ_t and σ_s , respectively, because the number of volumes n in the sequence is low (typically nine). It is important to understand that the main constraint in this application is the clinical limit on n . It might, therefore, seem attractive to compute the derivatives using a four-point central difference kernel or a four-dimensional (4-D) Sobel kernel (Table I), since if no presmoothing is used, $n = 5$, respectively, $n = 3$, are sufficient for these differentiation kernels. Indeed, these two are often used in the literature on 2-D optical flow computation, see for example [19]. However, in the 2-D case, their performance without prefiltering was found to be very low as a consequence of aliasing [1]. Performance might be improved by presmoothing with a Gaussian, but the temporal scale σ_t of the smoothing

kernel is then limited by n in the manner explained above. At a given sequence length n , the maximum of the temporal scale σ_t for a specific Gaussian derivative kernel (if the derivatives are computed using Gaussian derivatives) or Gaussian smoothing kernel (if they are computed using four-point central difference or Sobel kernels), is limited to $\sigma_{t\max}$

$$\begin{aligned}\sigma_{t\max}(\text{Gauss}) &= \frac{n-1}{6} \\ \sigma_{t\max}(\text{Sobel}) &= \frac{n-3}{6} \\ \sigma_{t\max}(\text{CD}) &= \frac{n-5}{6}\end{aligned}\quad (10)$$

provided the filter kernel is truncated to 3σ (resulting in a kernel of size $6\sigma + 1$). I.e., if $n = 9$, $\sigma_{t\max}(\text{Gauss}) = 1.33\dots$, $\sigma_{t\max}(\text{Sobel}) = 1$ and $\sigma_{t\max}(\text{CD}) = 0.66\dots$ In Section VI-A, we investigate the effect of the scale σ_t (at given n) on the performance of the optical flow algorithm with Gaussian derivatives and also compare the performance of the three derivative operators described above at given n , with $\sigma_{t\max}$ computed as in (10). The 4-D Sobel kernel is given in Table I

The algorithms were implemented in the Java language. A package with these implementations is available from www.isi.uu.nl/people/michael (please observe copyright and disclaimer statements).

IV. PERFORMANCE AND ACCURACY MEASUREMENTS

The true 3-D motion field \mathbf{v}_{ref} is known for the simulated and motion controlled sequences. The estimated 3-D motion vector \mathbf{v} is compared with \mathbf{v}_{ref} through an angular error measure, by a trivial generalization of the error formula of Barron, *et al.* [19]

$$\psi = \arccos(\hat{\mathbf{v}}_{\text{ref}} \cdot \hat{\mathbf{v}}) \quad (11)$$

where ψ denotes angular error, the difference between the correct and measured flow vector (reported in degrees), $\hat{\cdot}$ denotes normalization and \mathbf{v}_{ref} the true motion vector. Because motion vectors are expressed in space-time and errors can occur in the spatial (orientation) or temporal (magnitude) dimension or both, ψ , thus, conveniently expresses this combined error in a single number. We define the density as the number of reliable (i.e., if the smallest eigenvector is larger than a threshold τ) flow vectors divided by the total number of voxels in an image.

V. THREE-DIMENSIONAL MOTION VISUALIZATION

A. Background

In order to interpret the 3-D optical flow fields in relation to the anatomy of the orbit, it is helpful to display the flow fields together with a contour surface of the underlying soft tissue anatomy. We have used two methods: a stack of 2-D sections of the 3-D flow field laid over the anatomy also shown as a 2-D stack, and a 3-D volume rendering of the flow field together with a rendering of the static anatomy volume. Visualization of 3-D flow phenomena, as opposed to scalar volumes, is difficult and tends to produce complex images with heavily overlapping geometry [21]. Occlusion and depth ambiguities strain viewers' abilities to interpret the motion data. For example, arrow plots are generally not useful for 3-D flow,

since depth perception of one-dimensional (1-D) objects (the arrows) is poor compared with surface objects and populating three-space with arrows easily produces overloaded images. In addition, most approaches assume that the flow field is locally regular and dense [22]. A visualization method was developed to display the 3-D flow field of the motion of orbital tissues and still allow the relation to the underlying anatomy to be seen.

B. Two-Dimensional Section Visualization

We have previously found that color classification of 2-D motion vectors is effective in presenting the motion field in a compact manner, with both orientation and magnitude of the flow vector displayed in a single pixel [1]. However, color classification can sometimes make it difficult to see the orientation of the flow. Spot noise [23] and line integral convolution [24] are able to visualize regular and dense flow fields using textures formed of random noise oriented along the orientation of the flow vector. With these techniques, the noisiness of the texture makes it difficult to show the magnitude of the flow vector. Oriented line integral convolution (OLIC) allows the flow to be shown as separate small "traces," where the length of the trace corresponds to the velocity [25]. By coloring the "traces" or texture using our classification scheme, the advantages of both techniques are combined. The texture is formed by displaying 2-D elliptical Gaussians that are oriented in the direction of the flow vector. The pixel intensities of the texture are multiplied with the color resulting from classification of the magnitude of the flow vector at that pixel. Thus, both the orientation of the collective motion of a tissue and the orientation and magnitude of the motion of each individual pixel are visualized; see Fig. 2.

C. Three-Dimensional Volume Visualization

Particle visualization is a method whereby vectors are projected onto the image as small blurred ellipses oriented along the (projected) direction of motion [23]. We have adapted that method to show the flow field as a thinly transparent texture of colored particles that we have called *scintillations*. These are then projected over a surface rendering of the anatomical static 3-D MRI volume [22], [26]. Thus, the collective motion of a region of soft tissue can be appreciated as a texture and the individual motion vectors are still discernible.

The visualization proceeds as follows. While the static MRI volume is being rendered (involving voxel interpolation, gradient interpolation, opacity, shading, and viewplane compositing computations [26], [27] at all relevant volume locations), the interpolated 3-D flow vector corresponding with each volume location is also inspected. Only a jittered (i.e., pseudorandom on a grid) subset of vectors in the flow field is visualized to avoid cluttering. If a flow vector is reliable (see above) and to be visualized, the voxel at that location is not rendered. Instead, a scintillation ξ is projected onto the viewplane. A scintillation is a small, colored, elongated, oriented half-ovoid Gaussian with parameters ξ_c , its color, ξ_s , its shape, and ξ_o , its opacity.

The color ξ_c of the scintillation is determined by classification of the 3-D motion vector according to a 3-D generalization of the scheme adopted in [1]: the color is cast into HSV (hue, saturation, and value) [18] space by coding the magnitude $|\mathbf{v}|$ of

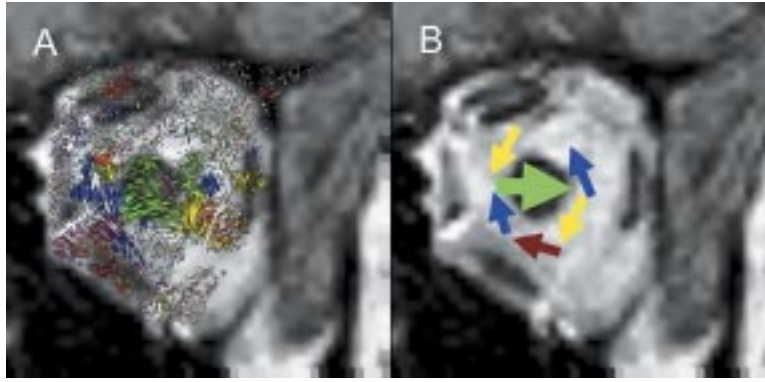


Fig. 2. 2-D section visualization. Shown is the motion of the intraconal tissue around the optic nerve in the apex of the orbit. (A) Flow field displayed over static MRI of the left orbit (coronal view). (B) Schematic view of motion as explanation of (A). The colors of the motion vectors in (A). The green arrow indicates the motion of the optic nerve (the front of the eye is gazing in the opposite direction), while the tissue in front of the optic nerve is moving out of its way and the tissue behind the optic nerve fills in the gap left behind; see, also, Fig. 8.

the motion vector into the saturation channel and the 2-D orientation (along a specified axis in 3-D) into the hue channel. Faster motion shows as brighter colors.

The shape ξ_s of the scintillation is determined by classification of the 3-D motion vector. The length of the half-ovoid is dependent on the magnitude $|\mathbf{u}|$ of the 2-D projection of the flow vector \mathbf{v} onto the viewplane. Faster motion, thus, shows as more elongated scintillations. The elongation effect of the scintillation is determined by a scaling factor σ_l . Only half of the resulting ovoid is shown. As $|\mathbf{u}|$ approaches zero, the scintillations become round dots, the size of which is determined by the standard deviation of (the associated probability function of) a Gaussian, σ_d . The computation of ξ_s is as follows:

$$\begin{aligned} \mathbf{U}_h &= \mathbf{M}\mathbf{V}_h \\ \varepsilon_1 &= u_i p_i - u_j p_j \\ \varepsilon_2 &= u_j p_i + u_i p_j \\ \sigma_l &= \sigma_d + \sigma_s |\mathbf{u}| \\ \xi_s(p_i, p_j) &= e^{-((\varepsilon_1^2/\sigma_s^2) + (\varepsilon_2^2/\sigma_l^2))}, \text{ if } \varepsilon_2 > 0 \\ \xi_s(p_i, p_j) &= 0, \text{ otherwise} \end{aligned} \quad (12)$$

where \mathbf{M} = a 4×4 projection transformation matrix (relating homogeneous voxel coordinates to projection viewplane coordinates), $\mathbf{V}_h = (\mathbf{v}_x, \mathbf{v}_y, \mathbf{v}_z, 1)^T$ i.e., \mathbf{v} in homogeneous coordinates, $\mathbf{U}_h = (\mathbf{u}_i, \mathbf{u}_j, \mathbf{u}_k, \mathbf{u}_l)^T$ the projection of the motion vector onto the viewplane (in homogeneous coordinates), ε_1 and ε_2 the short and long axes of the half-ovoid, ξ_s = the scintillation shape, $\mathbf{p} = (p_i, p_j)$ a point in ξ_s , $\mathbf{u} = (\mathbf{u}_i, \mathbf{u}_j)^T$, σ_d the standard deviation of a Gaussian determining the minimum length and width of the ovoid and σ_l a scaling factor determining the effect of \mathbf{U} on the length of the major axis of ξ_s .

The opacity ξ_o defines how transparent the scintillation is. If the flow field is not sparse, depth differences between scintillations need to be accentuated to allow individual scintillations to be discerned [28]. In order to accomplish this effect, an opaque halo is rendered around every scintillation by manipulating the opacity, ξ_o . ξ_o is a 2-D Gaussian with a standard deviation σ_h that defines the length of its short axis, with $\sigma_h > \sigma_s$

$$\xi_o(p_i, p_j) = |\mathbf{v}| \left(e^{-((\varepsilon_1^2/\sigma_h^2) + (\varepsilon_2^2/\sigma_l^2))} \right). \quad (13)$$

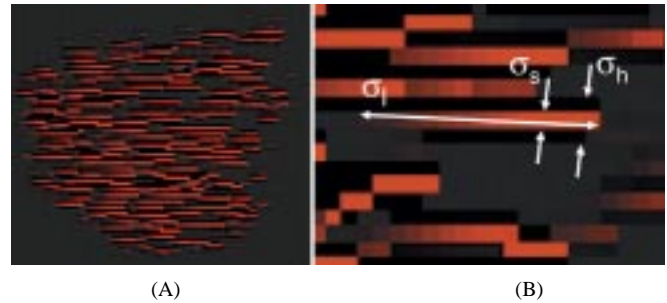


Fig. 3. Example of scintillations. (A) Texture formed by multiple scintillations. The underlying motion field is a translation to the right (seen from the back) with an average motion of 1.0 voxel/volume (frame). The hue and orientation of the scintillations code for the direction of the flow vector, while the length of the half-ovoid and the saturation of its color code for the magnitude of the flow vector. The background has been made dark-gray and the underlying static object is not shown on purpose. (B) Detail of scintillation. Shown are the parameters that define the shape of a scintillation and its halo: σ_s , the size of the short axis of the half-ovoid (here, 0.4), σ_l the scaling factor for the long axis, and σ_h the size of the short axis of the halo (here, 0.7).

Thus, a tiny dark opaque halo is created around a scintillation, to make individual vectors discernible [29], [30]. The approach is illustrated in Fig. 3.

VI. EXPERIMENTAL RESULTS

This section reports on the quantitative performance of the optical flow algorithm and shows visualizations of the 3-D motion fields obtained. For these experiments, the scale of the neighborhood Ω , σ_w , was set to the spatial scale at which the derivatives were computed or at which Gaussian smoothing was performed, i.e $\sigma_w = \sigma_s$. $\sigma_s = 1.3$ in all experiments described in this paper while the voxel dimensions are $0.8 \times 0.8 \times 2.0$ mm. Therefore, the scale of the neighborhood Ω is approximately $4.8 \times 4.8 \times 12.0$ mm, corresponding to the scale of the moving and deforming structures in the orbit, that ranges from approximately 4–5 mm (optic nerve cross-section) to 40 mm (rectus muscle length) in size in any one dimension. The results in Sections VI-A and B are meant to be compared with the results in Barron, *et al.* [19] study and our previous 2-D study [1], so that we chose the same values for τ (0, 1, respectively, 5), to maximize the comparability.

TABLE II
PERFORMANCE ON *CUBE* USING GAUSSIAN DERIVATIVES AT SCALE $\sigma_t = 1.3$
(IN OTHER WORDS, NINE VOLUMES WERE NEEDED IN THE SEQUENCE) AT
DIFFERENT THRESHOLDS τ . IN ALL EXPERIMENTS, $\sigma_s = \sigma_w = 1.3$

	Angular Error ψ	Standard Dev	Density
$\tau=0$	10.56°	20.59°	67.86%
$\tau=1$	0.54°	0.27°	8.10%
$\tau=5$	0.48°	0.23°	3.87%

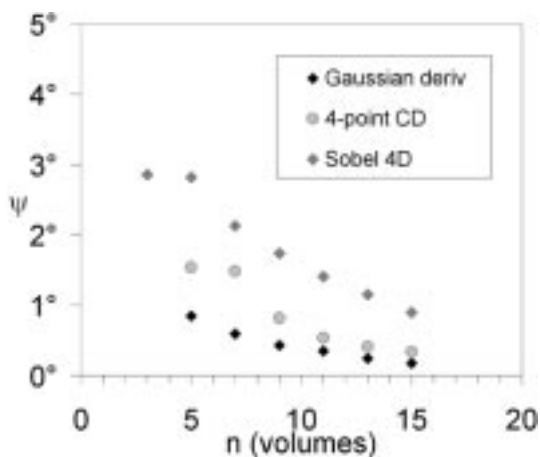


Fig. 4. Performance of the 3-D algorithm on *Cube* expressed as angular error ψ (in degrees) as a function of temporal scale σ_t of either the Gaussian derivatives or Gaussian prefiltering; $\sigma_r = \sigma_w = 1.2$ and $\tau = 5$.

A. Synthetic Sequences

The first experiment was designed to check the reliability of the 3-D optical flow computation and compare its performance to that of the Lucas and Kanade algorithm on the *Square2* sequence (a simulated motion sequence formed of a blurred black square on a white background moving at (1.3, 1.3) pixels per frame) as found by Barron, *et al.* [19]. The *Cube* sequence was created as the 3-D equivalent of *Square2* and has a motion of (1.33, 1.33, 1.33) voxels per volume, i.e., to the upper-right-back. [See Fig. 1(A) for a single slice from a single volume].

Table II summarizes the performance of the algorithm on *Cube* using Gaussian derivatives at different thresholds τ . The performance is comparable to that of the Lucas and Kanade algorithm on *Square2*: at $\tau = 1$, the average error was $0.21^\circ \pm 0.16^\circ$ (at a density of 7.9%) for *Square2*[19], while for *Cube* it is $0.54^\circ \pm 0.27^\circ$ (at a density of 8.10%).

As discussed above, an important constraint in this application is n , the number of volumes in a sequence. We have studied the effect of n on the performance (i.e., angular error ψ) of the algorithm with *Cube* and compared the effect of using Gaussian, central difference and Sobel derivative operators (the last two with Gaussian smoothing) at the maximum scale $\sigma_{t\max}$ allowed by n [see (10)], as shown in Fig. 4. With *Cube*, Gaussian derivatives for gradient estimation perform superior to the others

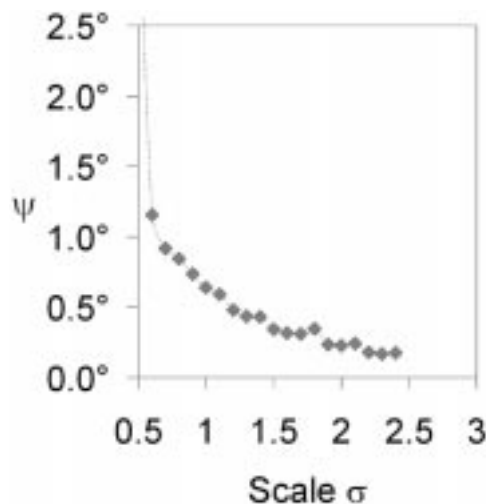


Fig. 5. Performance of the 3-D optical flow algorithm expressed as angular error ψ (in degrees) as a function of the temporal scale σ_t of the Gaussian derivatives, $\tau = 5$.

given n and have reasonable performance even at $n = 5$ (when $\sigma_{t\max} = 0.66\dots$). We have also studied the performance of the algorithm, using Gaussian derivatives, in terms of temporal scale space on the *Cube* sequence; see Fig. 5. At a temporal scale $\sigma_t = 1.3$, which corresponds to $n = 9$, the angular error ψ is under 0.5° .

Fig. 6 shows a visualization of the flow field of *Cube* together with a rendering of the cube itself. The 3-D motion vectors can be determined only at the corners of the cube. The motion vectors show as blue-green scintillations and due to their halos, the flow vectors are separable and also visible as a semi-transparent texture.

B. MR Simulated and Measured Sequences

It is important to understand that since densities are expressed as a fraction of all voxels, densities of 0.1%–1% are actually not very sparse and still useful for this application.

Table III summarizes the main results of the algorithm on the *SteakSynth* hypervolume using Gaussian derivatives at different thresholds τ . *SteakSynth* was obtained by synthetic rotation of the steak volume [obtained by static MRI, Fig. 1(B)], with an angular rotation step of 5° per volume around the z axis. The decrease in performance compared with the *Cube* hypervolume is probably caused by the fact that the derivatives are more discontinuous due to the aliasing and partial volume effects of the MR acquisition process.

Table IV summarizes the main results for the *SteakDeform* hypervolume using Gaussian derivatives and various thresholds τ . *SteakDeform* was obtained by synthetic nonrigid 3-D deformation of the steak volume [obtained by static MRI, Fig. 1(B)] using a simulated rigid ball and supporting plane. The better performance compared with *SteakSynth* is caused by the more regular differences in the magnitude of the deformation (over space), compared with the more rapid magnitude differences (over space) of a rotation.

Table V summarizes the main results for the *SteakMR* hypervolume. *SteakMR* was obtained by rotating the steak at 5° per volume (around the z axis) and acquiring an MRI volume

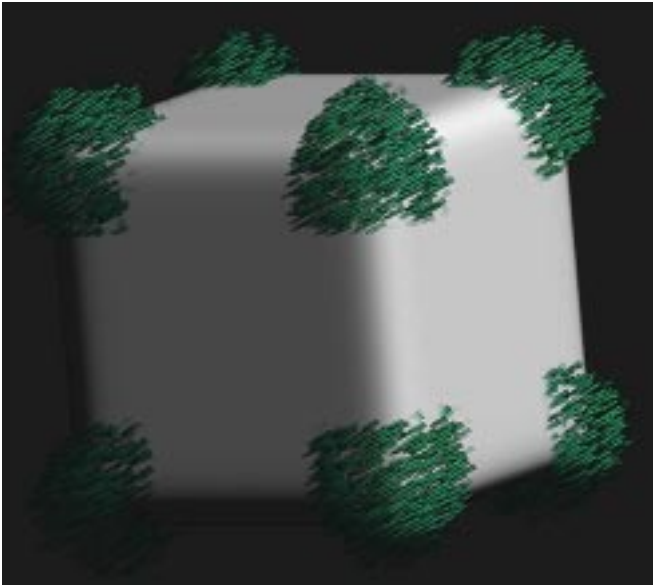


Fig. 6. Scintillation rendering of the 3-D flow field of *Cube* combined with a rendering of the cube itself. The cube is translating at (1.3, 1.3, 1.3) voxels per volume (to the upper-right-back). $\sigma_t = 1.3$, $\tau = 5$. Motion is visible only at the corners of the cube.

TABLE III
PERFORMANCE ON *STEAKSYNTH* WITH $n = 9$, GAUSSIAN DERIVATIVES AT TEMPORAL SCALE $\sigma_t = 1.3$, FOR DIFFERENT THRESHOLDS τ

	Angular Error ψ	Standard Dev	Density
$\tau=0$	7.55°	8.25°	77.92%
$\tau=1$	4.29°	3.19°	5.03%
$\tau=5$	3.99°	1.65°	0.09%

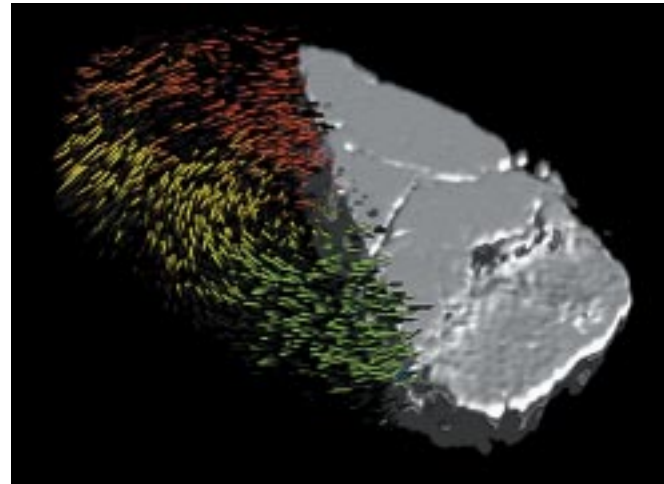
TABLE IV
PERFORMANCE ON *STEAKDEFORM* WITH GAUSSIAN DERIVATIVES AT SCALE $\sigma_t = 1.3$, FOR DIFFERENT THRESHOLDS τ

	Angular Error ψ	Standard Dev	Density
$\tau=0$	4.79°	8.34°	74.79%
$\tau=1$	1.76°	2.20°	30.05%
$\tau=5$	1.66°	2.53°	12.09%

at each step. Compared to *SteakSynth*, performance of the algorithm has deteriorated. This is probably caused by aliasing in the temporal dimension caused by partial volume effects and the anisotropic phase effect of the orientation of the tissue relative

TABLE V
PERFORMANCE ON *STEAKMR* WITH $n = 9$, GAUSSIAN DERIVATIVES AT SCALE $\sigma_t = 1.3$, FOR DIFFERENT THRESHOLDS τ . SINCE DENSITIES ARE SO LOW AT $\tau = 5$, RESULTS ARE ALSO GIVEN FOR $\tau = 0.5$ AND $\tau = 2.5$

	Angular Error ψ	Standard Dev	Density
$\tau=0$	18.43°	16.18°	97.00%
$\tau=0.5$	16.02°	11.41°	9.60%
$\tau=1$	12.26°	7.26°	3.45%
$\tau=2.5$	7.13°	3.42°	0.32%
$\tau=5$	3.91°	1.66°	0.01%



(a) (b)

Fig. 7. (A) Scintillation rendering of the 3-D motion field of *SteakMR* combined with (B) a volume rendering of the "anatomy" of the steak. The anatomy under the motion field is not shown since the motion field is too dense. The axis of rotation is oriented perpendicular to the surface of the steak. Gaussian derivatives, $\sigma_t = 1.3$, $\tau = 2.5$.

to the gradient of the MR field. Since the density at $\tau = 5$ is smaller than 0.01%, which is not very useful for our purposes, results are also reported for intermediate thresholds $\tau = 0.5$ and $\tau = 2.5$.

Fig. 7 shows a scintillation rendering of one half of the flow field of *SteakMR* together with the anatomy of the steak for the other half.

C. MR Measured Orbital Sequences

We have used 3-D optical flow computation to determine the motion as a function of gaze position in hypervolumes of the orbit, *OrbitMR*. Since the true motion field v_{ref} is unknown in this case, it is impossible to obtain quantitative data on performance. We found that the obtained 3-D flow fields are similar to those obtained using 2-D optical flow estimation along different planes.

To evaluate the clinical usefulness of 3-D motion estimation, we have tried to measure the 3-D motion of the *intraconal* tissue. The intraconal tissue is the fatty and fibrous tissue located in

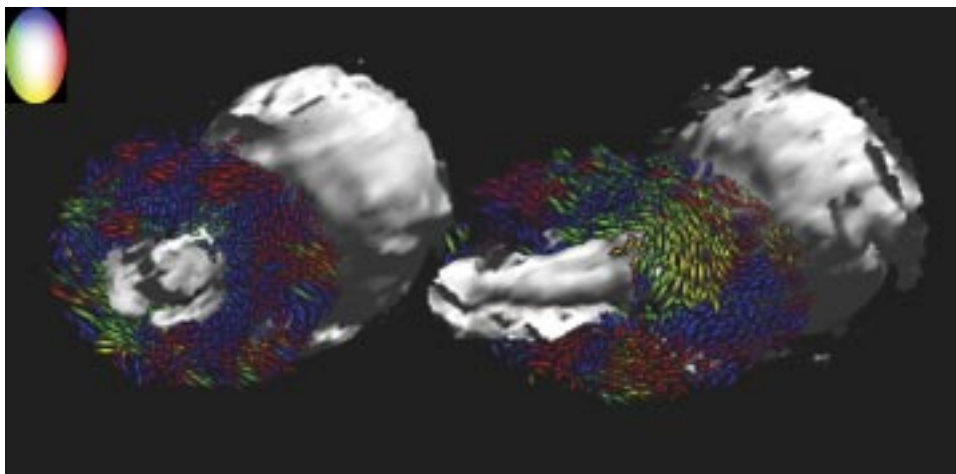


Fig. 8. Scintillation rendering of the 3-D motion field of *OrbitMR*, together with a static rendering of both globes and both optic nerves. Shown as seen from inside the skull looking forward toward globes (right is right). Only the motion field of the intraconal tissue close to the optic nerve is displayed, because it would otherwise be obscured by the motion of the rectus muscles and other tissues. The subject is gazing from left to right and the optic nerve (at the back of the globe), therefore, moves in the opposite direction, to the left. The motion of the intraconal tissue is coupled to that of the optic nerve above and below it (green, i.e., to the left). At the trailing edge of the right optic nerve (right in this figure) this tissue can be seen to fill the space left by the motion path of the nerve. From the top of the nerve it fills in a *downward* direction (yellow) and from the bottom of the nerve it fills in an *upward* direction (blue). This is best seen around the right nerve. The index in the upper left corner shows the orientations corresponding to the colors. $\sigma_t = 1.3$, $\tau = 2.5$.

between the extraocular muscles, around the optic nerve, and is composed of tiny globules of fat suspended between connective tissue septa [31]. Since the space within the orbital cavity is fixed, this tissue has to deform when the muscles and the globe move during gaze. The kinematics are unknown, but are relevant since it has recently been proposed that this tissue may form a functional skeleton for the orbital contents [32]. The 3-D motion field of the intraconal tissue was measured in three subjects. One of the motion fields, with the subject gazing from left to right, is shown in 2-D in Fig. 2 and in a scintillation rendering in Fig. 8. The intraconal fat can be seen to deform from over and under the optic nerve into the space left by it as it trails the movement of the globe. This tissue, thus, fills the vacuum left by the nerve, as behind a spoon moving through syrup. Therefore, it deforms like a liquid and less like a solid (if it deformed in the manner of more solid matter such as a sponge, it would have deformed in the same direction as the nerve, filling up the space from sideways instead of from top and bottom).

VII. DISCUSSION

This paper introduces a 3-D optical flow algorithm and a 3-D optical flow visualization technique to quantify and visualize objectively the 3-D motion of soft tissues in the orbit from MR volume sequences. In addition, it studies the quality of the motion fields obtained, given the clinical constraints on sequence length and resolution. The Lucas and Kanade algorithm [33] was generalized to three dimensions and tested on (4-D) motion sequence hypervolumes of synthetic motion of a stylized object (a cube), of synthetic motion of an MR imaged natural object (a steak), of an MR imaged rotating natural object (the same steak) and of MR imaged motion in the human orbit during gaze. The 3-D motion field was visualized by rendering color-textured 2-D slices with the 2-D motion and also by scintillation rendering, so as to display the 3-D motion field together with conventional volume rendering of the underlying (static) anatomy.

Previous approaches to 3-D optical flow estimation have been successful in determining 3-D motion and deformation from 3-D volumetric CT and MR sequences of the human heart [34] and the human brain [35], [36]. Human cardiac optical flow computation from CT sequences has been rigorously validated [36]. These approaches are based on 3-D generalizations of Horn and Schunk's algorithm, using a global smoothness constraint on the motion field [17]. Local smoothness constraints, such as Lucas and Kanade's algorithm [19], where the flow is constrained to be regular only in the neighborhood of the point where the optical flow vector is to be determined, were found to give better and more robust performance in 2-D optical flow estimation in both natural scenes [19] and in MR sequences [1].

Our results indicate that 3-D optical flow computation by the algorithm introduced in this study is feasible. Its performance on synthetic 3-D volume sequences is comparable to that obtained by conventional 2-D optical flow measurement algorithms on 2-D sequences. The algorithm is sensitive to the quality of the partial derivatives and the best performance was reached using Gaussian derivatives. The performance on realistic MR volume sequences is quite acceptable. The derived flow fields are of sufficient quality for clinical purposes. In fact, we have been able to measure the previously unknown kinematics of the intraconal tissue, which was found to deform like a liquid and less like a solid. Compared to Cine PC and tagged MR, 3-D optical flow computation has the advantage of needing only the intensity data (instead of phase data for three axes in the case of cine PC) and would also work for cine CT. The relative advantages and disadvantages of the three techniques merit further study.

The results also show that 3-D optical flow visualization by scintillation rendering, combined with surface rendering of anatomy, gives an insight into the relation of tissue motion with the underlying anatomy. This allows an evaluation of the quality of the 3-D flow field when the true flow field is not known.

In conclusion, 3-D optical flow computation has sufficient performance to estimate the motion of soft tissues in the orbit for clinical purposes and scintillation rendering is effective in understanding the relationship between tissue motion and underlying anatomy.

ACKNOWLEDGMENT

The authors would like to thank the anonymous reviewers for their valuable comments to two earlier versions of this paper. They would also like to thank W. Bartels, Ph.D., for the use of his MR rotation device and K. Vincken, Ph.D., for his help in setting up the website.

REFERENCES

- [1] M. D. Abramoff, W. J. Niessen, and M. A. Viergever, "Objective quantification of the motion of soft tissues in the orbit," *IEEE Trans. Med. Imag.*, vol. 19, pp. 986–995, Oct. 2000.
- [2] M. D. Abramoff, A. P. Van Gils, G. H. Jansen, and M. P. Mourits, "MRI dynamic color mapping: A new quantitative technique for imaging soft tissue motion in the orbit," *Investigat. Ophthalmol. Vis. Sci.*, vol. 41, no. 11, pp. 3256–3260, Oct. 2000.
- [3] J. G. H. Lasudry, B. N. Lemke, L. R. Gentry, and B. S. Sires, "Multipositional high-resolution imaging of the human orbit's functional anatomy," *Orbit*, vol. 16, no. 3, pp. 159–184, 1997.
- [4] J. L. Demer and J. E. Miller, "Orbital imaging in strabismus surgery," in *Clinical Strabismus Management*, A. L. Rosenbaum and A. P. Santiago, Eds. Philadelphia, PA: Saunders, 1999, pp. 84–98.
- [5] J. M. Miller, "Functional anatomy of normal human rectus muscles," *Vis. Res.*, vol. 29, pp. 223–240, 1989.
- [6] F. T. Sheehan, F. E. Zajac, and J. E. Drace, "Using cine phase contrast magnetic resonance imaging to noninvasively study *in vivo* knee dynamics," *J. Biomech.*, vol. 31, no. 1, pp. 21–26, Jan. 1998.
- [7] E. A. Zerhouni, D. M. Parish, W. J. Rogers, A. Yang, and E. P. Shapiro, "Human heart: Tagging with MR imaging—A method for noninvasive assessment of myocardial motion," *Radiology*, vol. 169, no. 1, pp. 59–63, Oct. 1988.
- [8] N. J. Pelc, R. J. Herfkens, A. Shimakawa, and D. R. Enzmann, "Phase contrast cine magnetic resonance imaging," *Magn. Reson. Q.*, vol. 7, no. 4, pp. 229–254, Oct. 1991.
- [9] C. J. Bakker, M. J. Hartkamp, and W. P. Mali, "Measuring blood flow by nontriggered 2D phase-contrast MR angiography," *Magn. Reson. Imag.*, vol. 14, no. 6, pp. 609–614, 1996.
- [10] M. Drangova, Y. Zhu, B. Bowman, and N. J. Pelc, "*In vitro* verification of myocardial motion tracking from phase-contrast velocity data," *Magn. Reson. Imag.*, vol. 16, no. 8, pp. 863–870, Oct. 1998.
- [11] J. L. Prince, S. N. Gupta, and N. F. Osman, "Bandpass optical flow for tagged MRI," *Med. Phys.*, vol. 27, no. 1, pp. 108–118, Jan. 2000.
- [12] L. Florack, W. Niessen, and M. Nielsen, "The intrinsic structure of optic flow incorporating measurement duality," *Int. J. Comput. Vis.*, vol. 27, no. 3, pp. 263–286, 1998.
- [13] S. C. Amartur and H. J. Vesselle, "A new approach to study cardiac motion: The optical flow of cine MR images," *Magn. Reson. Med.*, vol. 29, no. 1, pp. 59–67, 1993.
- [14] T. S. Denney and J. L. Prince, "A frequency domain performance analysis of Horn and Schunk's optical flow algorithm for deformable motion," *IEEE Trans. Image Processing*, vol. 4, pp. 1324–1328, Sept. 2000.
- [15] G. P. Zientara, P. Saiviroonporn, P. R. Morrison, M. P. Fried, S. G. Hushek, R. Kikinis, and F. A. Jolesz, "MRI monitoring of laser ablation using optical flow," *J. Magn. Reson. Imag.*, vol. 8, no. 6, pp. 1306–1318, 1998.
- [16] L. Dougherty, J. C. Asmuth, A. S. Blom, L. Axel, and R. Kumar, "Validation of an optical flow method for tag displacement estimation," *IEEE Trans. Med. Imag.*, vol. 18, pp. 359–363, Apr. 1999.
- [17] B. K. P. Horn and B. G. Schunk, "Determining optical flow," *Artif. Intell.*, vol. 17, pp. 185–204, 1981.
- [18] K. R. Castleman, *Digital Image Processing*. Englewood Cliffs, NJ: Prentice-Hall, 1996.
- [19] J. L. Barron, D. J. Fleet, and S. S. Beauchemin, "Performance of optical flow techniques," *Int. J. Comput. Vis.*, vol. 12, no. 1, pp. 43–77, 1994.
- [20] W. J. Niessen, J. S. Duncan, M. Nielsen, L. M. J. Florack, and B. M. ter Harr Romeny, "A multiscale approach to image sequence analysis," *Comput. Vis. Image Understand*, vol. 65, no. 2, pp. 259–268, 1997.
- [21] N. Max, R. Crawfis, and C. Grant, "Visualizing 3D velocity fields near contour surfaces," in *IEEE Visualization 94*, pp. 248–255.
- [22] D. C. Banks, "Illumination in diverse codimensions," *Comput. Graph.*, vol. 28, pp. 327–334, 1994.
- [23] J. J. v. Wijk, "Spot noise—Texture synthesis for data visualization," *Comput. Graph.*, vol. 25, no. 4, pp. 309–318, 1991.
- [24] B. Cabral and L. Leedom, "Imaging vector fields using line integral convolution," in *Comput. Graph.*, Proc. SIGGRAPH 1993, 1993, pp. 263–270.
- [25] R. Wegenkittl and E. Groller, "Fast oriented line integral convolution for vector field visualization via internet," in *Proc. IEEE Visualization '97*, Phoenix, AZ, pp. 309–315.
- [26] M. Levoy, "Display of surfaces from volume data," *Comput. Graph. Applicat.*, vol. 8, no. 3, pp. 29–37, 1988.
- [27] B. Lichtenbelt, R. Crane, and S. Naqvi, *Introduction to Volume Rendering*. Englewood Cliffs, NJ: Prentice-Hall, 1998.
- [28] V. Interrante and Ch. Grosch, "Strategies for effectively visualizing 3D flow with volume LIC," in *Proc. IEEE Visualization '97*, Phoenix, AZ, 1997, pp. 421–424.
- [29] J. J. Koenderink, "Relief: Pictorial and otherwise," *Image Vis. Computing*, vol. 13, no. 5, pp. 321–334, 1995.
- [30] D. Dooley and M. F. Cohen, "Automatic illustration of 3D geometric models: Lines," *Comput. Graph.*, vol. 24, no. 2, pp. 77–82, 1990.
- [31] L. Koornneef, "Orbital septa: Anatomy and function," *Ophthalmology*, vol. 86, pp. 876–880, 1979.
- [32] M. D. Abramoff, M. A. Viergever, and M. Ph. Mourits, "Recti muscle pulleys and decompression surgery for Graves' orbitopathy [ARVO abstract]," *Investigat. Ophthalm. Vis. Sci.*, vol. 41, no. 4, p. 738, 2000.
- [33] B. Lucas and T. Kanade, "An iterative image registration technique with an application to stereo vision," in *Proc. DARPA Image Understanding Workshop*, Washington, DC, 1981, pp. 121–130.
- [34] S. M. Song and R. M. Leahy, "Computation of 3-D velocity fields from 3-D cine CT images of a human heart," *IEEE Trans. Med. Imag.*, vol. 10, pp. 295–306, Sept. 1991.
- [35] N. Hata, A. Nabavi, W. M. Wells, S. K. Warfield, R. Kikinis, P. M. Black, and F. A. Jolesz, "Three-dimensional optical flow method for measurement of volumetric brain deformation from intraoperative MR images," *J. Comput. Assist. Tomogr.*, vol. 24, no. 4, pp. 531–538, July 2000.
- [36] J. M. Gorce, D. Friboulet, and I. E. Magnin, "Estimation of three-dimensional cardiac velocity fields: Assessment of a differential method and application to three-dimensional CT data," *Med. Image Anal.*, vol. 1, no. 3, pp. 245–261, 1997.